Magnetic surface topology in decaying plasma knots

Smiet, C.B.; Thompson, A.; Bouwmeester, P.; Bouwmeester, D.

PAPER • OPEN ACCESS

Magnetic surface topology in decaying plasma knots

To cite this article: C B Smiet *et al* 2017 *New J. Phys.* **19** 023046

New Journal of Physics
The open access journal at the forefront of physics

Deutsche Physikalische Gesellschaft DPG
IOP Institute of Physics

Published in partnership with: Deutsche Physikalische Gesellschaft and the Institute of Physics

OPEN ACCESS

RECEIVED
22 September 2016

REVISED
29 December 2016

ACCEPTED FOR PUBLICATION
2 February 2017

PUBLISHED
23 February 2017

PAPER

Magnetic surface topology in decaying plasma knots

C B Smiet[1,3], A Thompson[2], P Bouwmeester[1] and D Bouwmeester[1,2]

[1] Huygens-Kamerlingh Onnes Laboratory, Leiden University, PO Box 9504, 2300 RA Leiden, The Netherlands
[2] Department of Physics, University of California Santa Barbara, Santa Barbara, CA 93106, United States of America
[3] Author to whom any correspondence should be addressed.

E-mail: smiet@physics.leidenuniv.nl

Keywords: magnetic topology, magnetic helicity, magnetic reconnection, topological solitons

Abstract

Torus-knot solitons have recently been formulated as solutions to the ideal incompressible magnetohydrodynamics (MHD) equations. We investigate numerically how these fields evolve in resistive, compressible, and viscous MHD. We find that certain decaying plasma torus knots exhibit magnetic surfaces that are topologically distinct from a torus. The evolution is predominantly determined by a persistent zero line in the field present when the poloidal winding number $n_p \neq 1$. Dependence on the toroidal winding number n_t is less pronounced as the zero line induced is contractible and disappears. The persistent zero line intersects the new magnetic surfaces such that, through the Hopf–Poincaré index theorem, the sum of zeroes on the new surfaces equals their (in general non-zero) Euler characteristic. Furthermore we observe the formation of magnetic islands between the surfaces. These novel persistent magnetic structures are of interest for plasma confinement, soliton dynamics and the study of dynamical systems in general.

It is remarkable how abstract topological concepts are directly relevant to many branches of science. A prime example is the Hopf map [1], a non-trivial topological structure that has found applications in liquid crystals [2], molecular biology [3], superconductors [4], superfluids [5], Bose–Einstein condensates [6, 7], ferromagnets [8], optics [9–11], and plasma physics [12, 13]. This article deals with topological aspects of novel persistent plasma configurations that emerge from decaying plasma torus knots.

Due to the generally high electrical conductivity of plasma described by magnetohydrodynamics (MHD), large electrical currents can flow and plasmas are heavily influenced by the resulting magnetic forces. The zero-divergence magnetic fields can lead to closed magnetic field lines, field lines that ergodically fill a magnetic surface, and field lines that chaotically fill a region of space. In ideal (zero-resistance) MHD the magnetic flux through a perfect conducting fluid element cannot change, leading to frozen in magnetic fields in the plasma [14]. This implies that in ideal MHD magnetic topology and magnetic helicity is conserved [15–17].

In 1982 Kamchatnov described an intrinsically stable plasma configuration [13] with a magnetic topology based on fibers of the Hopf map [18]. This type of MHD equilibrium, where the fluid velocity is parallel to the field and equal to the local Alfvén speed, was shown by Chandrasekhar to be stable [19], even in specific cases in the presence of dissipative forces [20]. Quasi stable self-organizing magnetic fields with similar magnetic topology to Kamchatnov's field (but different flow) have recently been demonstrated to occur in full-MHD simulations [12]. Here the final configuration is not a Taylor state, which is consistent with recent findings in [21].

Recently the class of topologically non-trivial solutions to Maxwell's equations has been extended by including torus knotted fields [22]. Another way of obtaining such solutions, for massless fields of various spins, is to use twistor theory [23]. The magnetic fields of the $t = 0$ solutions in [22], have been used to construct novel plasma torus knots [24], solutions to the ideal incompressible MHD equations.

To investigate the potential importance of plasma torus knots for realistic plasma the influence of dissipation has to be investigated. Dissipation can lead to breaking and reconnection of field lines and thereby change the magnetic topology. In this article we show numerically that novel persistent magnetic structures emerge that are characterized by a non-zero Euler characteristic. Through the Poincareé Hopf index theorem this leads to

precise statements about zeroes in the magnetic fields which further clarifies the plasma structures. Furthermore magnetic islands are observed in between the new magnetic surfaces.

1. Plasma torus knots

An ideal MHD soliton, as defined in [13, 24], is a static configuration of magnetic field $\boldsymbol{B}$, fluid velocity $\boldsymbol{u}$, and pressure p that satisfies the ideal, incompressible MHD equations. The fluid field and pressure that solve this can be inferred from the momentum equation, which can be written as:

$$\frac{\partial \boldsymbol{u}}{\partial t} + \boldsymbol{u}\cdot\nabla\boldsymbol{u} - \frac{1}{\rho}\boldsymbol{B}\cdot\nabla\boldsymbol{B} + \frac{1}{\rho}\nabla\left(p + \frac{B^2}{2}\right) = 0, \tag{1}$$

and the induction equation:

$$\frac{\partial \boldsymbol{B}}{\partial t} = \nabla\times(\boldsymbol{u}\times\boldsymbol{B}). \tag{2}$$

In the ideal and incompressible case the fluid field and pressure corresponding to the soliton are given by

$$\boldsymbol{u} = \pm\frac{\boldsymbol{B}}{\sqrt{\rho}}, \quad p = p_\infty - \frac{B^2}{2}, \tag{3}$$

respectively. Already in 1956 in a paper titled 'On the stability of the simplest solution of the equations of hydromagnetics', Chandrasekhar noted that this represents an *exact stationary solution* and proved it to be stable against linear perturbations [19].

Kamchatnov analyzed this solution for the specific case where the magnetic field and velocity field are given by the Hopf map, every single field line is linked with every other. The static magnetic field of the Kamchatnov–Hopf soliton, whose magnetic field is identical to the $t = 0$ magnetic field of an electromagnetic solution in free space [9] can be obtained in various ways. Bateman's construction [25] of describing a (null) electromagnetic field via two Euler potentials α and β such that $\boldsymbol{F} = \boldsymbol{E} + \mathrm{i}\boldsymbol{B} = \nabla\alpha\times\nabla\beta$, is well suited to generate new solutions to Maxwells equations with torus knotted field lines [22]. The class of torus knot solitons, of which the Kamchatnov–Hopf soliton is an element, are the solutions to the ideal MHD equations where the velocity and fluid field are identical to the magnetic field of these EM solutions [24].

The torus knot solitons are constructed using the following complex-valued Euler potentials

$$\alpha = \frac{r^2 - 1 + 2\mathrm{i}z}{r^2 + 1}, \text{ and } \beta = \frac{2(x - \mathrm{i}y)}{r^2 + 1}, \tag{4}$$

followed by a substitution $r \to r/r_0$ (where $r^2 = x^2 + y^2 + z^2$) to rescale the configuration. Taking $\mathrm{Im}\,[\nabla\alpha\times\nabla\beta]$ gives the magnetic field of the Kamchatnov–Hopf soliton. Generalizing this construction by raising α to a positive integer power n_t which we call the toroidal integer, and β to a positive integer power n_p which we call the poloidal integer, the magnetic field of a $(n_\mathrm{t},\ n_\mathrm{p})$ plasma torus knot is obtained via:

$$\boldsymbol{B} = \frac{c\ \mathrm{Im}[\nabla\alpha^{n_\mathrm{t}}\times\nabla\beta^{n_\mathrm{p}}]}{\sqrt{a}}, \tag{5}$$

where c is a scaling constant with correct dimensions and $a = \int(\mathrm{Im}[\nabla\alpha^{n_\mathrm{t}}\times\nabla\beta^{n_\mathrm{p}}])^2\,\mathrm{d}^3x$, integrated over all space, is a normalization factor that provides all magnetic field configurations with the same magnetic energy.

As noted, the plasma (1, 1) torus knot is the Kamchatnov–Hopf soliton: every magnetic field line is a circle that is linked with every other field line. Otherwise the field configuration is characterized by a finite set of core field lines that each form an $(n_\mathrm{t},\ n_\mathrm{p})$ torus knot and around which other field lines span nested magnetic surfaces [22, 24]. Figures 1(a) and (b) show an example of a plasma torus knot magnetic field configuration with toroidal integer $n_\mathrm{t} = 3$ and a poloidal integer $n_\mathrm{p} = 2$. Figure 1(a) shows that there are two core field lines that each form a (3, 2) torus knot, and figure 1(b) shows two magnetic surfaces spanned by field lines close to the two core field lines.

The magnetic helicity, defined as

$$h_\mathrm{m} = \int\boldsymbol{A}\cdot\boldsymbol{B}\mathrm{d}^3x, \tag{6}$$

(where $\boldsymbol{A}$ is defined through $\boldsymbol{B} = \nabla\times\boldsymbol{A}$) is an invariant of ideal MHD. The total magnetic helicity of the plasma torus knots is found by integrating equation (6) over all space, and is given by

$$h_\mathrm{m} = -\frac{r_0}{n_\mathrm{t} + n_\mathrm{p}}, \tag{7}$$

where we have used $\boldsymbol{A} = c\ \mathrm{Im}[\beta\nabla\alpha]/\sqrt{a}$. The magnetic field of the torus knots goes to zero at infinity, such that this helicity is gauge invariant. The magnetic helicity is reduced in the plasma torus knots with higher values

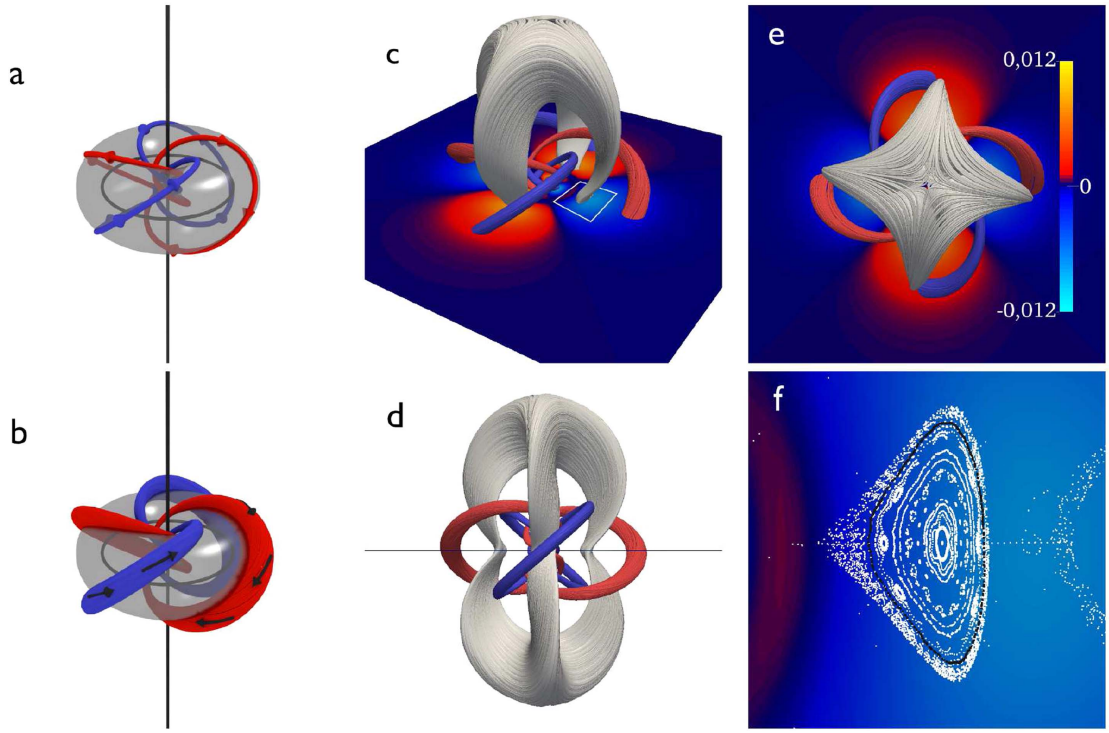

Figure 1. New magnetic surfaces and their relation to the structure in the initial $n_t = 3$ and $n_p = 2$ plasma torus knot. (a) The original plasma torus knot structure consists of two core field lines that form (3, 2) torus knots. (b) Other field lines form magnetic surfaces around one of the two core field lines,. The black lines indicate the zero lines in the field. The new magnetic surface forms between the two core field lines, as shown from angled view (c), side view (d) and top view (e). Magnetic surfaces with the field line topology of the original field are shown in red and blue, the new surface in gray. The plane at $z = 0$ shows the z-component of the magnetic field (scale bar given in panel (e)). (f) Poincaré plot of the magnetic structure inside the non-toroidal surfaces, showing nested surfaces, as well as magnetic islands. The white square in panel (c) indicates the size of the region in panel (f).

of n_p and n_t. This reduction is qualitatively understood by noting that the core field lines trace a path around the torus with a left-handed writhe while the magnetic surfaces have a right-handed twist around the core field lines. Since both writhe and twist contribute to the helicity the opposite signs cancel each other [26, 27] and higher values of toroidal and poloidal integers reduce the total magnetic helicity.

The conservation of energy, angular momentum, and magnetic helicity, can provide stability to certain plasma configurations. As shown in [24] only the plasma torus knots with $n_p = 1$ have non-zero angular momentum and are able to form stable configurations in ideal MHD. We now investigate the solutions represented by equations (3) and (5) in the case of a non-ideal plasma by adding compressibility, magnetic diffusivity, and viscosity.

2. New emerging surfaces

We numerically study the dynamics of plasma torus knots using the PENCIL code, a high-order finite difference code for compressible MHD [28, 29]. In resistive MHD the l.h.s. of equation (1) gains a viscous term $-\boldsymbol{F}_{\rm visc}$ and the r.h.s. of equation (2) gains a resistive term $-\nabla \times \eta(\nabla \times \boldsymbol{B})$. In the compressible case the density ρ is calculated by a continuity equation, and an isothermal equation of state is used such that $p = c_s^2 \rho$. The equations solved and the details of how the resistive terms are implemented are described in appendix A. The characteristic length is set to $r_0 = 1/2l_0$ and the simulation box size is $(2\pi l_0)^3$ with 256^3 grid points. The viscosity and magnetic diffusivity were set to $\nu = \eta = 2 \times 10^{-4}$, giving a Prandtl number of unity.

We observe a dramatic change in the magnetic topology during a rapid first phase in the dynamics characterized by field lines pinching off and reconnecting. During this reconfiguration new magnetic surfaces are formed which have in general a different topology. After this first phase the new configurations persist in time and have an unchanging magnetic topology and a decreasing field strength due to the finite resistivity. For example figures 1(c)–(e) give an angled view, a side view, and a top view of a new magnetic surface in the (3, 2) plasma torus knot.

The magnetic fields close to the center of the initial plasma configuration have strong components in opposite directions along the z axis. The dynamical principle of the formation of the new surfaces is that regions

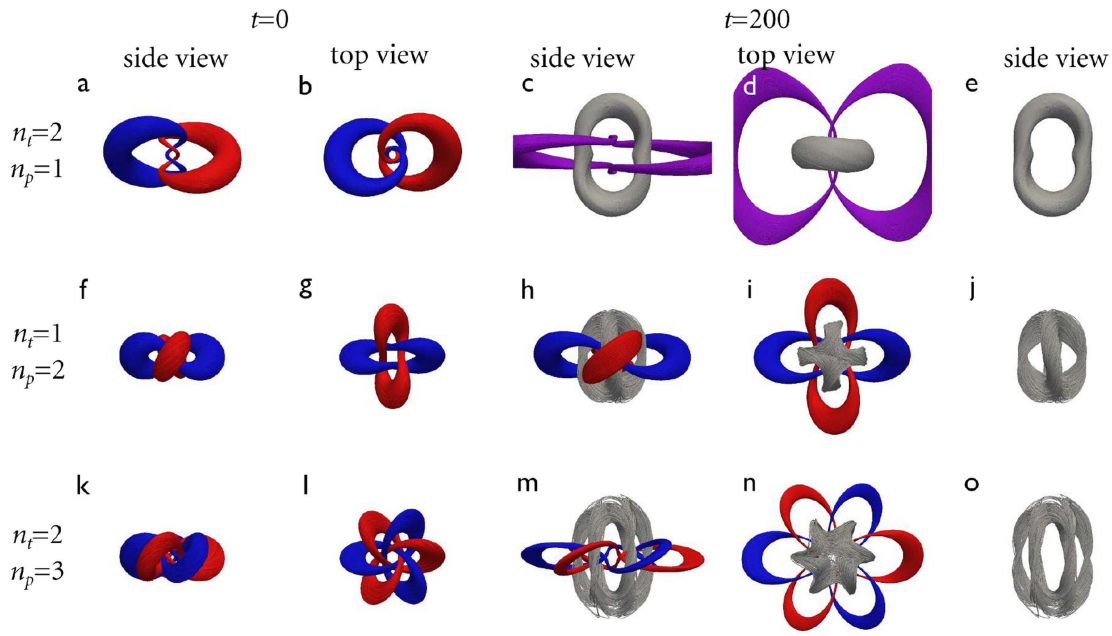

Figure 2. Initial and emerging magnetic surfaces. First column: side view (along x-axis) of magnetic surfaces at $t = 0$. Second column: top view at $t = 0$. Third column: side view at $t = 200$, where both new magnetic surfaces (gray) and the remains of the original magnetic surfaces can be seen. Fourth column: top view at $t = 200$. Fifth column: only the new magnetic surfaces. The initial magnetic surfaces are colored in red and blue, while magnetic surfaces that were not initially present are colored gray. The magnetic surfaces in figures (a) and (b) can be seen to recombine into the single magnetic surface shown in figures (d) and (e) (purple).

of largest counter propagating fields (here the center of the configuration) will have highest dissipation which pinches off field lines. The remaining part of the field lines will find nearby pinched-off fields lines with whom they connect resulting in the new magnetic surfaces.

An interesting interpretation of the emergence of the observed structures is given by the mechanism of the flow of helicity across scales as demonstrated by Scheeler *et al* in [30]. They show that the component of fluid helicity caused by the linking of vorticity filaments in fluids will, through localized reconnections translate to larger scale writhe, and eventually to twist, present on the largest scale, approximately conserving total helicity. The parallels between fluid and magnetic helicity have been established since their conception [15]. In this interpretation the effect of the localized reconnection at the center of the configuration can be seen as removing the writhing and linking of the initial magnetic surfaces, resulting in a configuration where helicity is present as twist in the antiparallel legs of the new magnetic structure.

The topology of a surface is characterized by its genus g, which is equal to the number of holes in that surface. A torus has only one hole, and therefore genus 1, but the new (gray) emerging surface is a surface with three holes, a triple torus. The genus of a surface is related to the Euler characteristic by $\chi = 2 - 2g$, which is an important topological invariant. The Poincaré–Hopf index theorem relates the Euler characteristic to zero points of a vector field on the surface as we shall show in section 4 and is therefore an important quantity in analyzing the new plasma structures.

The new surface drawn in gray is part of a set of nested surfaces with the same topology. This can be seen from the Poincaré plot in figure 2(f). Note that there also appear, as expected from references [12, 31], magnetic islands (see the section on islands).

Simulations have been performed for the nine combinations with $n_\mathrm{t} = 1, 2, 3$ and $n_\mathrm{p} = 1, 2, 3$. Figure 2 shows the results for $(n_\mathrm{t}, n_\mathrm{p})$ equal to (2, 1), (1, 2) and (2, 3).

The configurations with $n_\mathrm{p} = 1$ all reconfigure in a way such that a new set of toroidal nested surfaces appear. The relation between this new set (shown in gray) and the original two sets can be seen for $n_\mathrm{p} = 1$, $n_\mathrm{t} = 2$ in figures 2(c)–(e), and is such that the new surfaces are tori lying in the x, z-plane. The original (red and blue) surfaces have merged into the purple surface, and will eventually disappear from the simulation. Most notably however, when $n_\mathrm{p} \geqslant 1$ we observe magnetic surfaces that are not topologically a torus, but a triple torus as seen in figures 2(h)–(j), and a quintuple torus in figures 2(m)–(o). These new surfaces are shown at simulation time $t = 200$, to illustrate their relationship to the original magnetic surfaces. At later times in the simulation the original surfaces will disappear , and only the surfaces with the new magnetic topology persist.

The created surface depends on n_p directly. When $n_\mathrm{p} = 1$ the new surface is a torus, when $n_\mathrm{p} = 2$ a triple torus ($g = 3$), and when $n_\mathrm{p} = 3$ a surface which has genus $g = 5$. These magnetic surfaces consist of $2n_\mathrm{p}$ twisted

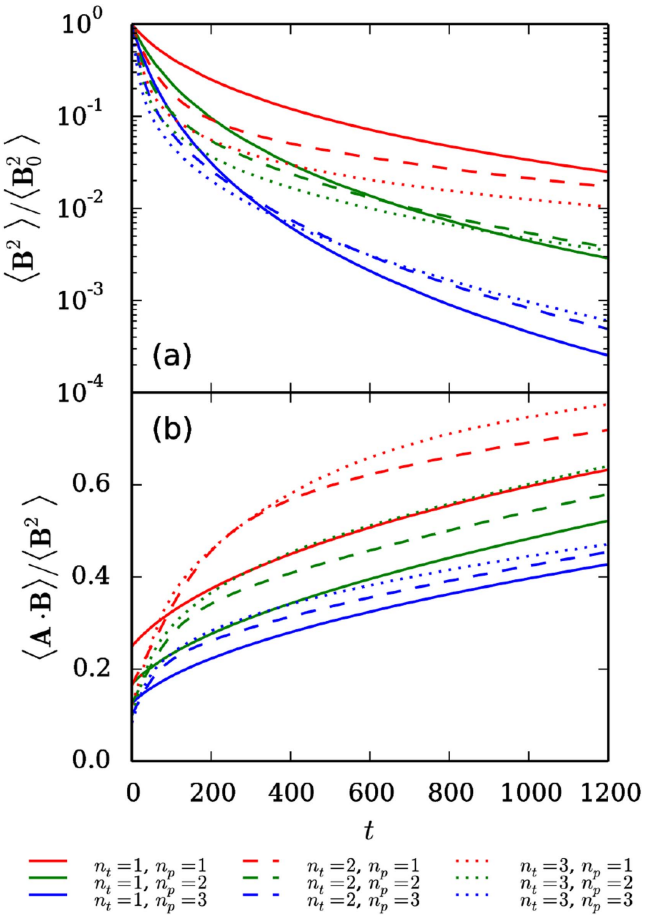

Figure 3. Decay of magnetic energy for all plasma torus knots with n_t and n_p ranging from 1 to 3. (a) Magnetic field strength as a function of time. It is clear that the higher values of n_p decay faster. Initially higher values of n_t decay faster as well, but this trend reverses with sufficient time. (b) Normalized magnetic helicity as a function of time.

'legs' that run parallel to the z-axis. These legs meet on the z-axis above and below the $z = 0$ plane. In half the legs the magnetic field is oriented in the positive z-direction, in the other half in the negative z-direction. Where the legs meet the field exhibits a magnetic cusp geometry and the field lines switch over from one leg to the other.

3. Magnetic decay

If we look at the time evolution of the mean magnetic energy $\langle \boldsymbol{B}^2 \rangle / \langle \boldsymbol{B}_0^2 \rangle$, shown in figure 3, we see that the configurations with $n_p = 1$ (red curves) show the lowest energy loss, and thus the highest stability, followed by the fields with $n_p = 2$, and finally the fields with $n_p = 3$. The lowest loss of energy for fields where $n_p = 1$ is consistent with the analytical stability analysis in [24] that predicts plasma torus knots with $n_p = 1$ to be stable. Figure 3(b) shows the evolution of normalized magnetic helicity (magnetic helicity divided by magnetic energy). Because the fields start out normalized by energy, their initial value corresponds with the result of equation (7). The increase in normalized magnetic helicity can be seen as the result of the magnetic energy decaying faster than the helicity.

We observe that during the entire simulation the fluid velocity $\boldsymbol{u}$ remains to a high degree parallel and equal in (dimensionless) magnitude to the magnetic field $\boldsymbol{B}$, even as the magnetic topology changes. The stability of the configuration is predicated on this condition being maintained. Balancing the momentum equation in this way is fundamentally different from the stability exhibited by a solution to the Grad Shafranov equation [32] or a force-free field [14].

4. Zero lines

The initial fields of the plasma torus knots contain nonsingular points where the magnetic field strength vanishes if either n_p or n_t is not unity. This can easily be seen by expanding equation (5) into:

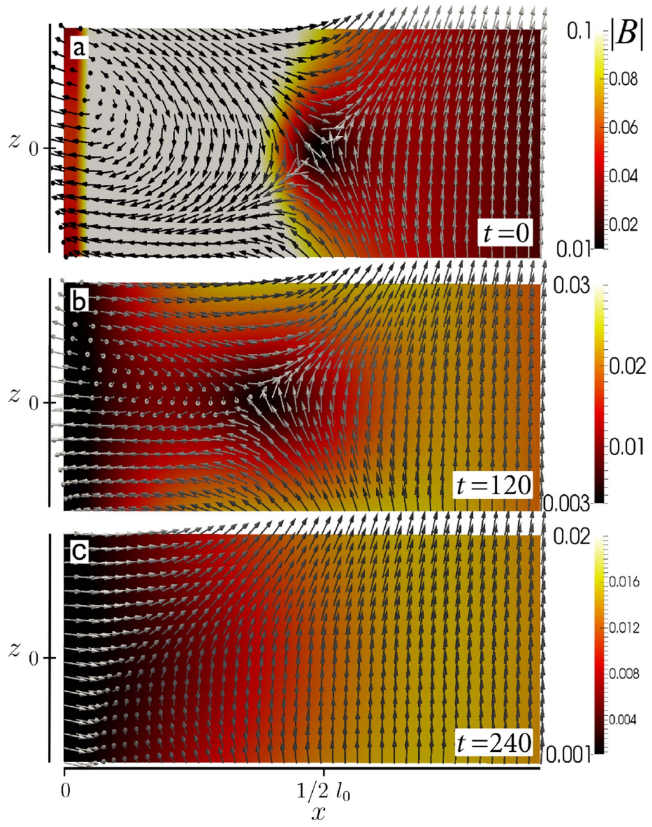

Figure 4. Cut through the x–z plane showing the disappearance of the circular null line. (a) Initial field, (b) field at time $t = 120$, and (c) disappearance of the null line by merging with the straight null on the z-axis at $t = 240$.

$$\boldsymbol{B} = \frac{c\,\mathrm{Im}[(n_\mathrm{t}\alpha^{n_\mathrm{t}-1}n_\mathrm{p}\beta^{n_\mathrm{p}-1})\nabla\alpha \times \nabla\beta]}{\sqrt{a}}, \tag{8}$$

which goes to zero at any point where $\alpha = 0$ if n_t is not 1, or where $\beta = 0$ if n_p is not 1. This gives rise to vortex nulls in the field via the method described [33]. For $n_\mathrm{t} \neq 1$ the field vanishes on the circle in the $z = 0$ plane $\{(x, y, z)|z = 0, x^2 + y^2 = r_0\}$, and for $n_\mathrm{p} \neq 1$ the field vanishes along the entire z-axis. The field only approaches zero linearly around the circular null if n_t is two, and similarly for the straight null if $n_\mathrm{p} = 2$, otherwise the null is higher-order.

Null points have been described extensively in the literature [34, 35] because of their role in reconnection [36]. We analyze the null lines in the field using the method presented in [35], by constructing the linearization matrix $\mathbf{M}$ whose indices are given by $M_{ij} = \partial_j B_i$, (see appendix B). The field around a null can be characterized by the three eigenvectors of this matrix [35] that represent the directions from which field lines approach and leave the null. Around the null lines, these three vectors are orthogonal, with the zero-eigenvalue eigenvector in the direction of the null line. The other two vectors determine two orthogonal directions, one from which the magnetic field lines approach the null, and the other determines the direction in which field lines leave the null. These two vectors rotate around the zero line as one moves along the zero line. The number of rotations of these vectors around the straight null is n_t, and the number of rotations around the circular null is n_p (see appendix B).

The zero circle disappears by contracting to a point on the origin. This process is shown in figure 4, and it explains why the final configuration depends predominantly on the poloidal index n_p, which determines the topology of the new magnetic surfaces.

The Poincaré–Hopf index theorem states that the sum of the indices of the zeroes of a vector field on a compact, oriented manifold is equal to the Euler characteristic χ of that manifold. A magnetic surface is such a manifold, and the magnetic field necessarily is a vector field in that surface. A toroidal surface ($\chi = 0$) allows a smooth vector field without any zero points. A magnetic surface can only form the observed triple torus ($\chi = -4$), or quintuple torus ($\chi = -8$) if there are points where the magnetic field is zero, and the indices of these zeroes then must sum to -4 or -8, respectively. These zeroes are provided by the zero line on the z-axis, that intersects the surfaces exactly four times and carries index -1 or -2 (where the index is defined by the field restricted to the two-dimensional surface perpendicular to the zero line) if $n_\mathrm{p} = 2$ or $n_\mathrm{p} = 3$, respectively. Therefore these surfaces can exist by grace of the zero line, and they can only persist if the zero line persists.

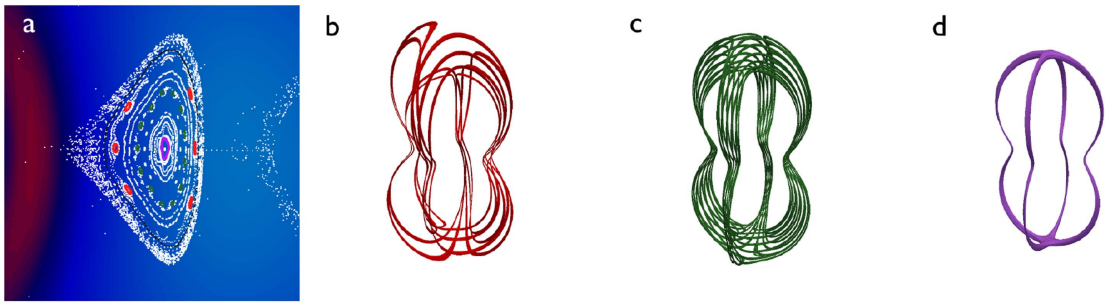

Figure 5. Magnetic surfaces and islands in the region with the new magnetic surfaces. (a) The Poincaré map of the region, indicating where the magnetic islands in (b) (red), (c) (green), and an inner surface with the same topology as the set of islands (d) (purple) are located in the nested set of surfaces.

It is generally assumed that extended zeroes areunstable [17, 35, 37]. In our simulations however we observe that if the magnetic field starts at zero on the straight null, this zero line persists during entire simulation. This is in contrast to the zero line on thecircle in the $z = 0$ plane, which disappears quickly, and is not present in the final configuration, as is shown in figure 4.

The Poincaré–Hopf index of a nonsingular zero point can be defined, as for example in [38]. Here it is shown that the vector field on the boundary of a neighborhood of the nonsingular null can be extended to a field in the interior of that neighborhood with finitely many singular nulls, and the sum of these indices is defined as the total index of the null. The total sum of the indices of nonsingular nulls is equal to the Euler characteristic of the manifold in which these nulls reside. The Euler characteristic of $\mathbb{R}^3$ is 0, and therefore the indices of the null lines sum to zero. This explains how the zero on thecircle can contract to a point, and disappear, leaving no zero point behind, or merge with the null line on the z-axis.

The null on the z-axis does not move, and persists in time. This does not necessarily imply that the zero line is stable, as any external perturbation of the form $\epsilon \boldsymbol{B}_z$ will make the null disappear, but the internal plasma dynamics do not make the null disappear. This persistence can be understood as a consequence of the symmetry of the field around the z-axis. The symmetry of the matrix $\mathbf{M}$ entails that the eigenvectors of $\mathbf{M}$ are orthogonal around the zero line, such that the field approaches the null from two orthogonal directions, in a plane perpendicular to the null line. The restriction of the vector field to this two-dimensional plane has a topological singularity (an X-point), and we observe that no field in the z-direction is created, allowing the zero line to persist, and the non-toroidal surfaces to exist.

5. Magnetic islands

The new magnetic surfaces are part of a set of nested surfaces with the same topology. There are, similar as what is observed from breaking up of toroidal magnetic surfaces [12, 31], also magnetic islands between these surfaces. Between the non-toroidal magnetic surfaces these islands can take very different, and complicated forms, tracing out intricate knots and links in the space between the intact non-toroidal surfaces (see figure 5).

Magnetic islands are generally described by casting magnetic field line flow in terms of a Hamiltonian dynamical system, and the magnetic surfaces are invariant tori in this system. In the unperturbed system, the field will consist only of nested toroidal surfaces characterized by a rotational transform. A perturbation will cause some tori to break up into island chains. Close to rational surfaces, (surfaces where the rotational transform is rational, i.e. field lines form closed curves) field lines will form surfaces that lie around one of the closed field lines of the original rational surface.

The islands in these non-toroidal surfaces also originate from an intact surface, as can be seen in figure 5(a). The field in the cross section of one upwards oriented 'leg' of the branched surface rotates, and then is split over the two downwards oriented legs, to be split and combined again. Because of this a rotational transform of the surface cannot be defined. Even though every point of the cross section will eventually map back to the cross section, this mapping is not necessarily continuous, and not in general a rotation. We do observe field structures that strongly resemble magnetic islands, but these island chains need not be symmetrically distributed across the surface, as is the case for the structure in figure 5(b). Because these islands form around a field line lying on a non-toroidal surface, their path need not be a torus knot, but can follow a differently knotted path.

6. Conclusions and discussion

We have studied a class of plasma torus knots in resistive plasma, which consist of linked and knotted core field lines surrounded by nested toroidal surfaces. n_p has strongest influence on the time evolution of these structures. Large values for n_t slow down the decrease of $\langle \boldsymbol{B}^2 \rangle$ only at high t. These dynamics can be understood by the dynamics of the zero lines, where the circular null, caused by $n_\mathrm{t} > 1$ is able to contract to a point and disappear, but the straight null caused by $n_\mathrm{p} > 1$ persists, and allows for new magnetic ordering with low energy loss.

In the resistive simulations the magnetic topology is not conserved, and new and interesting magnetic topologies are created. Structures with genus 3 and 5 are observed, and persist in the simulations. These structures also exhibit magnetic island formation, which has a different character to islands that emerge from toroidal magnetic surfaces.

Given the crucial role played by the extended zero in the plasma configuration resulting from initial symmetry, it seems unlikely that magnetic surfaces with non-zero Euler characteristic occur in the turbulent plasmas encountered in an astrophysical context. It is however possible to engineer this symmetry. A zero line can occur where sets of opposing fields meet, and can be created by sets of opposing coils, as is done in the cusp geometry [39]. These non-toroidal surfaces suggest new topologies for magnetic confinement fusion devices, essentially a marriage of the cusp fusion concept [39] or polywell fusion concept [40] and the stellarator concept [41].

Acknowledgments

The authors would like to acknowledge Jan Willem Dalhuisen, Joost Opschoor, Joe Swearngin, Simon Candelaresi, Roland van der Veen, Gunnar Hornig, David Pontin and Keith Moffatt for stimulating discussions and invaluable feedback. This work is supported by NWO VICI 680-47-604, NSF Award PHY-1206118 and the NWO graduate programme.

Appendix A. Equations solved

The expressions for the initial conditions in the simulations were generated from equation (5) using Mathematica. The source for the PENCIL-CODE is freely available on http://pencil-code.nordita.org/.

To simulate the plasma dynamics we assume an isothermal plasma, we take the background pressure to be the pressure for an isothermal gas $p = \rho c_\mathrm{s}^2$, where ρ is the density and c_s^2 is the speed of sound squared. We solve the coupled equations in terms of $\boldsymbol{u}$, ρ, and $\boldsymbol{A}$, from which the magnetic field is calculated by $\boldsymbol{B} = \nabla \times \boldsymbol{A}$. The vector potential of the initial condition is calculated by $\boldsymbol{j} = \nabla \times \boldsymbol{B}$ and transforming that to the vector potential using the inverse Laplace transform.

The equation of motion for an isothermal plasma is

$$\frac{D\boldsymbol{u}}{Dt} = -c_\mathrm{s}^2 \nabla \ln \rho + \boldsymbol{j} \times \boldsymbol{B} \Big/ \rho + \boldsymbol{F}_\mathrm{visc}, \tag{A.1}$$

where $\boldsymbol{u}$ is the fluid velocity, $\frac{D}{Dt} \equiv \frac{\partial}{\partial t} + \boldsymbol{u} \cdot \nabla$ is the convective derivative, and $\boldsymbol{j} = \nabla \times \boldsymbol{B}$. The viscous force is

$$\boldsymbol{F}_\mathrm{visc} = \rho^{-1} \nabla \cdot 2\nu\rho \mathbf{S}, \tag{A.2}$$

where ν is the kinematic viscosity and $\mathbf{S}$ is the traceless rate of strain tensor $S_{ij} = \frac{1}{2}(u_{i,j} + u_{j,i}) - \frac{1}{3}\delta_{ij} \nabla \cdot \boldsymbol{u}$. The continuity equation in terms of the logarithmic density has the form

$$\frac{D \ln \rho}{Dt} = -\nabla \cdot \boldsymbol{u}. \tag{A.3}$$

The induction equationcan be written terms of the vector potential as

$$\frac{\partial \boldsymbol{A}}{\partial t} = \boldsymbol{u} \times \boldsymbol{B} + \eta \nabla^2 \boldsymbol{A}, \tag{A.4}$$

where η is the magnetic diffusivity.

The PENCIL-code solves equations (A.1), (A.3), and (A.4) using finite-difference methods to sixth-order in space and third-order in time. The simulation domain is a square box of size $(2\pi l_0)^3$ with 256^3 mesh points and open boundary conditions. Simulations with periodic boundary conditions were also performed, and seen to behave identically. The open boundary conditions are enforced by imposing vertical fields ($\boldsymbol{u}$, $\boldsymbol{B}$) at the boundary, allowing field to escape the simulation volume, and a constant first derivative of the density across the boundary.

All quantities are calculated using dimensionless units. The isothermal sound speed c_s, set is set to 1. The fluid velocity is set parallel to the magnetic field vector to satisfy equation (1), and the density is calculated from $\rho = p/c_s^2$ using the pressure from equation (3) with $p_\infty = 1$. The magnetic field is calculated from equation (5), with the constant c generally set to 0.25, but changed to a lower value if the simulation became unstable for the fields at higher values of n_t and n_p. It was verified that time evolution is independent of this scaling. The fields were scaled to a characteristic length $r_0 = 1/2l_0$. The viscosity ν and magnetic diffusivity η were set to 2×10^{-4}.

Appendix B. Analysis of the zero lines

Here we analyze the null lines in the magnetic field of the initial plasma torus knots following [34, 35].

From the field around the position of the null line we construct the matrix $\mathbf{M}$ with elements $M_{ij} = \partial_j B_i$ so that the magnetic field can be expressed to lowest order as

$$\boldsymbol{B} = \mathbf{M} \cdot \boldsymbol{r}, \tag{B.1}$$

where $\boldsymbol{r} = (x, y, z)^T$ is the position vector. The properties of the field around the zero points are now encoded in this matrix [35]. For example, the sum of the diagonal elements $\partial_j B_j$ is equal to the divergence of $\boldsymbol{B}$, thus the trace of the matrix is zero. The eigenvectors of this matrix determine three important directions in space. Since we are investigating the field on a zero line there is at least one direction where $\mathbf{M} \cdot \boldsymbol{r} = 0$, where the field remains zero. This is the eigenvector of the matrix $\mathbf{M}$ with eigenvalue zero. The other two eigenvectors have opposite eigenvalues, and (when the eigenvalues are real) determine the direction in space from which the field lines approach the null and in which direction the field lines leave the null, so that the field exhibits an x-point configuration.

We are interested in analyzing the null points of the plasma torus knots. We start with the expression for an (n_t, n_p) plasma torus knot given by equation (3) in the main paper. Without loss of generality we can ignore the rescaling and drop the numerical pre-factors $\sqrt{a}$ and c so that the expression for B_i in index notation is given by:

$$B_i = \mathrm{Im}[(n_t \alpha^{n_t - 1} n_p \beta^{n_p - 1}) \epsilon_{ijk} (\partial_j \alpha)(\partial_k \beta)], \tag{B.2}$$

where we use the two complex-valued Euler potentials given in equation (4).

In the paper we describe how the magnetic field vanishes at points where α becomes zero if $n_t \neq 1$ and where β becomes zero if $n_p \neq 1$. These zeroes take the form of lines, with a zero line on the unit circle in the x, y-plane caused by the zero in α, and a straight zero line along the entire z-axis where β vanishes.

The element M_{ij} of the linearization matrix can be written using index notation as

$$\begin{aligned} M_{ij} = \partial_j B_i = \mathrm{Im}\,[n_t n_p \{ &(\partial_j [\alpha^{n_t - 1} \beta^{n_p - 1}])(\epsilon_{ikl} (\partial_k \alpha)(\partial_l \beta)) \\ &+ \alpha^{n_t} \beta^{n_p} (\partial_j (\epsilon_{ikl} (\partial_k \alpha)(\partial_l \beta))) \}]. \end{aligned} \tag{B.3}$$

Because we are evaluating this field at a point where α respectively β vanish, the second term in equation (B.3) is always zero. For the zero line on the unit circle (where $\alpha = 0$) the first term is only non-zero if the derivative of $\alpha^{n_t - 1}$ is non-zero, and the same holds for β if we look at the zero line on the z-axis. Thus if $n_t \geqslant 3$ there are no non-zero elements in $\mathbf{M}$ around the unit circle, and if $n_p \geqslant 3$ this holds for $\mathbf{M}$ evaluated on the z-axis. All the matrix elements are zero because the field does not approach zero linearly.

B.1. Eigenvectors of the straight null

If we focus on the on the z-axis where $\beta = 0$, in the case that $n_p = 2$, the matrix elements become:

$$M_{ij}|_{\beta=0} = \mathrm{Im}\,[n_t n_p \alpha^{n_t - 1} \partial_j \beta \boldsymbol{B}^i_{(1,1),\mathrm{compl}}], \tag{B.4}$$

where $\boldsymbol{B}_{(1,1),\mathrm{compl}} = \nabla\alpha \times \nabla\beta$, is the complex-valued vector field of the $(1, 1)$ plasma torus knot before taking the imaginary part. The linearization matrix on the z-axis becomes:

$$\mathbf{M} = n_t n_p \begin{pmatrix} \gamma & \delta & 0 \\ \delta & -\gamma & 0 \\ 0 & 0 & 0 \end{pmatrix}, \tag{B.5}$$

where γ is given by:

$$\gamma = \frac{8(2z \cos(\arg((\mathrm{i} + z)^2)(n_t - 1)) + (z^2 - 1)\sin(\arg((\mathrm{i} + z)^2)(n_t - 1)))n_p n_t}{(z^2 + 1)^4} \tag{B.6}$$

and δ is given by:

$$\delta = -\frac{8((z^2-1)\cos(\arg((\mathrm{i}+z)^2)(n_\mathrm{t}-1)) - 2z\sin(\arg((\mathrm{i}+z)^2)(n_\mathrm{t}-1)))n_\mathrm{p}n_\mathrm{t}}{(z^2+1)^4}. \tag{B.7}$$

The matrix $\mathbf{M}$ is symmetric, so the field around the null is characterized by three orthogonal eigenvectors, given by:

$$\boldsymbol{v}_1 = \begin{pmatrix} 0 \\ 0 \\ 1 \end{pmatrix}, \tag{B.8}$$

$$\boldsymbol{v}_2 = \begin{pmatrix} \frac{\gamma - \sqrt{\gamma^2+\delta^2}}{\delta} \\ 1 \\ 0 \end{pmatrix}, \tag{B.9}$$

$$\boldsymbol{v}_3 = \begin{pmatrix} \frac{\gamma + \sqrt{\gamma^2+\delta^2}}{\delta} \\ 1 \\ 0 \end{pmatrix}. \tag{B.10}$$

The respective eigenvalues are:

$$e_1 = 0, \tag{B.11}$$

$$e_2 = -\frac{8n_\mathrm{p}n_\mathrm{t}}{(z^2+1)^3}, \tag{B.12}$$

$$e_3 = \frac{8n_\mathrm{p}n_\mathrm{t}}{(z^2+1)^3}. \tag{B.13}$$

Here we have filled in the values of γ and δ.

The field around the z-axis is characterized by the null eigenvector in the z-direction indicating the direction of the null. The other two eigenvectors lie in the x, y-plane, with $\boldsymbol{v}_2$ determining the direction from which field lines approach the null line and $\boldsymbol{v}_3$ the direction in which field lines leave.

$\boldsymbol{v}_1$ and $\boldsymbol{v}_2$ are orthogonal in the x, y plane, and their direction depends on z. In order to determine the angle of these vectors in this plane as a function of z, we write the vector $\boldsymbol{v}_2$ as the complex number $\xi = \boldsymbol{v}_2^x + \mathrm{i}\boldsymbol{v}_2^y$, where the superscripts denote the x- respectively the y-component of the vector. After some manipulation we get:

$$\xi = \frac{2}{\mathrm{e}^{2\mathrm{i}\arg(z+\mathrm{i})n_\mathrm{t}} + \mathrm{i}} + 2\mathrm{i}. \tag{B.14}$$

The only z-dependence is given by the term $\arg(z+\mathrm{i})$ in the exponent in the denominator. As z passes from $-\infty$ to ∞ the value of $\arg(\mathrm{i}+z)$ varies smoothly from π to 0. This means that the value in exponent in the denominator varies from 0 to $2\pi n_\mathrm{t}$. Each time that $2\mathrm{i}\arg(z+\mathrm{i})n_\mathrm{t} = n3\pi/4$, the denominator becomes zero, and the real part of ξ goes from ∞ to $-\infty$. This happens exactly n_t times, and the imaginary part of ξ remains constant. Thus, the argument of ξ, and therefore the angle of the vector $\boldsymbol{v}_2$ with the x-axis then rotates an angle of πn_t as z goes from $-\infty$ to ∞.

Since by virtue of the symmetry of the matrix $\mathbf{M}$ the vector $\boldsymbol{v}_3$ is orthogonal to $\boldsymbol{v}_2$, the two vectors rotate around the z-axis (and lie in the x, y-plane) in the same direction, making exactly $n_\mathrm{p}/2$ full rotations as z goes from $-\infty$ to ∞. These two vectors determine the direction from which the field approaches and leaves the null, so the zero line is not a straightforward x-line, the directions from which field approach rotate, and the x-line null exhibits a twist over exactly $n_\mathrm{t}\pi$ degrees.

B.2. Eigenvectors of the circular null

We now focus on the zero line on the unit circle in the x, y-plane that is present in the plasma torus knots when $n_\mathrm{t} \neq 1$. This zero is characterized by the points where $\alpha = 0$. We choose the case where $n_\mathrm{t} = 2$ so the expression for the linearization matrix becomes:

$$M_{ij}|_{\alpha=0} = \mathrm{Im}\,[n_\mathrm{t}n_\mathrm{p}\beta^{n_\mathrm{p}-1}(\partial_j\alpha)\boldsymbol{B}^i_{(1,1),\mathrm{compl}}]. \tag{B.15}$$

For this calculation we use cylindrical coordinates, as we know that the null line, and thus one of the eigenvectors of $\mathbf{M}$ is oriented along the unit circle in the x, y plane, in the ϕ-direction. The matrix $\mathbf{M}$ in this basis (r, ϕ, z) then becomes:

$$\mathbf{M} = n_\mathrm{p} n_\mathrm{t} \begin{pmatrix} \sin(\phi - \arg(\mathrm{e}^{-\mathrm{i}\phi})(n_\mathrm{p}-1)) & 0 & -\cos(\phi - \arg(\mathrm{e}^{-\mathrm{i}\phi})(n_\mathrm{p}-1)) \\ 0 & 0 & 0 \\ -\cos(\phi - \arg(\mathrm{e}^{-\mathrm{i}\phi})(n_\mathrm{p}-1)) & 0 & -\sin(\phi - \arg(\mathrm{e}^{-\mathrm{i}\phi})(n_\mathrm{p}-1)) \end{pmatrix}. \tag{B.16}$$

The three eigenvalues (in the $(r,\ \phi,\ z)$-basis) are:

$$\boldsymbol{w}_1 = \begin{pmatrix} \sec(\phi - \arg(\mathrm{e}^{-\mathrm{i}\phi})(n_\mathrm{p}-1)) - \tan(\phi - \arg(\mathrm{e}^{-\mathrm{i}\phi})(n_\mathrm{p}-1)) \\ 0 \\ 1 \end{pmatrix}, \tag{B.17}$$

$$\boldsymbol{w}_2 = \begin{pmatrix} (1 + \sin(\phi - \arg(\mathrm{e}^{-\mathrm{i}\phi})(n_\mathrm{p}-1)))(-\sec(\phi - \arg(\mathrm{e}^{-\mathrm{i}\phi})(n_\mathrm{p}-1))) \\ 0 \\ 1 \end{pmatrix}, \tag{B.18}$$

$$\boldsymbol{w}_3 = \begin{pmatrix} 0 \\ 1 \\ 0 \end{pmatrix}, \tag{B.19}$$

where arg (ω) denotes the argument of the complex number ω. The respective eigenvalues of these eigenvectors are

$$e_{c1} = -n_\mathrm{p} n_\mathrm{t}, \tag{B.20}$$

$$e_{c2} = n_\mathrm{p} n_\mathrm{t}, \tag{B.21}$$

$$e_{c3} = 0. \tag{B.22}$$

The vector $\boldsymbol{w}_3$, with zero eigenvalue points in the ϕ-direction, the direction of the null line. The other two eigenvectors are perpendicular to that and orthogonal. We are again interested in the direction of these two vectors, as they determine the direction that field lines approach and leave the null.

We construct the complex number $\zeta = \boldsymbol{w}_1^r + \mathrm{i}\boldsymbol{w}_1^z$ from the vector $\boldsymbol{w}_1$. After some manipulation we find:

$$\zeta = \frac{2}{\mathrm{e}^{\mathrm{i}\phi n_\mathrm{p}} + \mathrm{i}} + 2\mathrm{i}. \tag{B.23}$$

Now the argument of the complex number ζ is equal to the angle that the vector $\boldsymbol{w}_1$ makes with the r-vector, and it varies as a function of the angular coordinate ϕ in our cylindrical coordinate system. In a full rotation around the circular null, ϕ goes from 0 to 2π. The denominator of $\frac{2}{\mathrm{e}^{\mathrm{i}\phi n_\mathrm{p}} + \mathrm{i}}$ passes zero every time $\mathrm{i}\phi n_\mathrm{p} = 3\pi/4$, which is exactly n_p times. This takes the real part of ζ from ∞ to $-\infty$ n_p times, whilst the imaginary part remains constant. Thus, the argument of ζ, and therefore the angle that the vector $\boldsymbol{w}_1$ makes with the r-vector in the $r,\ z$-plane makes a rotation of an angle of exactly $n_\mathrm{p}\pi$ in a full pass around the circular null.

The vector $\boldsymbol{w}_2$ is orthogonal to $\boldsymbol{w}_1$, and they signify the direction that field lines approach and leave the null. Also the circular null exhibits a twisted x-point geometry, with the direction of field line approach and the direction of field line departure rotating an angle of $n_\mathrm{p}\pi$ over the length of the null line.

References

[1] Urbantke H 2003 *J. Geom. Phys.* **46** 125–50
[2] Chen B G G, Ackerman P J, Alexander G P, Kamien R D and Smalyukh I I 2013 *Phys. Rev. Lett.* **110** 237801
[3] Monastyrsky M I 2007 *Topology in Molecular Biology* (Berlin: Springer)
[4] Ran Y, Hosur P and Vishwanath A 2011 *Phys. Rev.* B **84** 184501
[5] Volovik G E and Mineev V P 1977 *Sov. Phys.—JETP* **46** 401–4
[6] Kawaguchi Y, Nitta M and Ueda M 2008 *Phys. Rev. Lett.* **100** 180403
[7] Hall D S, Ray M W, Tiurev K, Ruokokoski E, Gheorghe A H and Möttönen M 2016 *Nat. Phys.* **12** 478–83
[8] Dzyloshinskii I E and Ivanov B A 1979 *JETP Lett.* **29** 540–2
[9] Rañada A F 1989 *Lett. Math. Phys.* **18** 97–106
[10] Irvine W T M and Bouwmeester D 2008 *Nat. Phys.* **4** 716–20
[11] Hoyos C, Sircar N and Sonnenschein J 2015 *J. Phys. A: Math. Theor.* **48** 255204
[12] Smiet C, Candelaresi S, Thompson A, Swearngin J, Dalhuisen J and Bouwmeester D 2015 *Phys. Rev. Lett.* **115** 095001
[13] Kamchatnov A M 1982 *Sov. Phys.—JETP* **55** 69–73
[14] Taylor J B 1974 *Phys. Rev. Lett.* **33** 1139
[15] Moffatt H K 1969 *J. Fluid Mech.* **35** 117–29
[16] Woltjer L 1958 *Proc. Natl Acad. Sci. USA* **44** 833
[17] Hornig G and Schindler K 1996 *Phys. Plasmas* **3** 781–91
[18] Hopf H 1931 *Math. Ann.* **104** 637–65
[19] Chandrasekhar S 1956 *Proc. Natl Acad. Sci.* **42** 273–6
[20] Kapur J and Jain R 1961 *Z. Astrophys.* **52** 110
[21] Moffatt H 2015 *J. Plasma Phys.* **81** 905810608
[22] Kedia H, Bialynicki-Birula I, Peralta-Salas D and Irvine W M T 2013 *Phys. Rev. Lett.* **111** 150404
[23] Thompson A, Wickes A, Swearngin J and Bouwmeester D 2015 *J. Phys. A: Math. Theor.* **48** 205202

[24] Thompson A, Swearngin J, Wickes A and Bouwmeester D 2014 *Phys. Rev.* E **89** 043104
[25] Bateman H 1915 *The Mathematical Analysis of Electrical and Optical Wave-motion on the Basis of Maxwell's Equations* (Cambridge: Cambridge University Press)
[26] Berger M and Field G B 1984 *J. Fluid Mech.* **147** 133–48
[27] Berger M A 1999 *Plasma Phys. Control. Fusion* **41** B167
[28] Brandenburg A and Dobler W 2002 *Comput. Phys. Commun.* **147** 471–5
[29] Haugen N E L, Brandenburg A and Dobler W 2004 *Phys. Rev.* E **70** 016308
[30] Scheeler M W, Kleckner D, Proment D, Kindlmann G L and Irvine W T 2014 *Proc. Natl Acad. Sci.* **111** 15350–5
[31] Hudson S, Dewar R, Dennis G, Hole M, McGann M, von Nessi G and Lazerson S 2012 *Phys. Plasmas* **19** 112502
[32] Shafranov V 1958 *Soviet Phys.—JETP* **6** 545
[33] Bialynicki-Birula I 2004 *J. Opt. A: Pure Appl. Opt.* **6** S181
[34] Lau Y T and Finn J M 1990 *Astrophys. J.* **350** 672–91
[35] Parnell C, Smith J, Neukirch T and Priest E 1996 *Phys. Plasmas* **3** 759–70
[36] Pontin D 2011 *Adv. Space Res.* **47** 1508–22
[37] Greene J M 1988 *J. Geophys. Res.: Space Phys.* **93** 8583–90
[38] Brasselet J P, Seade J and Suwa T 2009 *Vector Fields on Singular Varieties* vol 1987 (Berlin: Springer)
[39] Grad H 1961 Containment in cusped plasma systems *Technical Report* New York University, New York Institute of Mathematical Sciences
[40] Krall N A 1992 *Fusion Sci. Technol.* **22** 42–9
[41] Wakatani M 1998 *Stellarator and Heliotron Devices* vol 95 (Oxford : Oxford University Press)